Celestial Mechanics and Dynamical Astronomy (2024) 136:5
https://doi.org/10.1007/s10569-023-10171-2

ORIGINAL ARTICLE

Improved alpha shape-based continuum method for long-term density propagation

Pan Sun[1] · **Shuang Li**[2] · **Mirko Trisolini**[3] · **Camilla Colombo**[3]

Received: 21 April 2023 / Revised: 7 September 2023 / Accepted: 25 October 2023 /
Published online: 6 February 2024

Abstract

This paper presents an improved alpha shape-based linear interpolation method, and an improved binning method within the continuum method framework for accurate and efficient planar phase space long-term density propagation. The density evolution equation is formulated for the continuum density propagation under the influence of the solar radiation pressure and Earth's oblateness using semi-analytical equations. The concept of the alpha shape is included to get accurate interpolated density within the non-convex hull enclosing all the samples for the highly deformed and elongated density distribution. The improved binning method increases the density accuracy by considering the variant nonlinearity of the density within each alpha shape triangulation, which calculates the joint and marginal density as the weighted sum of density weights per bin area and per bin width, respectively. The suitable sample number for the continuum method and the suitable grid number for performing the linear interpolation are selected by trading off the density accuracy and the computational effort. The superiority of the improved alpha shape-based continuum method is demonstrated for accurate and efficient density propagation in the context of the high-altitude and high area-to-mass ratio satellite long-term propagation.

This article is part of the topical collection on Innovative computational methods in Dynamical Astronomy. Guest Editors: Christoph Lhotka, Giovanni F. Gronchi, Ugo Locatelli, Alessandra Celletti.

✉ Pan Sun
sunpan@czcit.edu.cn

✉ Shuang Li
lishuang@nuaa.edu.cn

Mirko Trisolini
mirko.trisolini@polimi.it

Camilla Colombo
camilla.colombo@polimi.it

[1] Department of Intelligent Equipment, Changzhou College of Information Technology, Changzhou, China

[2] Advanced Space Technology Laboratory, and College of Astronautics, Nanjing University of Aeronautics and Astronautics, Nanjing, China

[3] Department of Aerospace Science and Technology, Polytechnic University of Milan, Milan, Italy

Keywords Density propagation · Density evolution equation · Semi-analytical equation · Alpha shape · Linear interpolation · Improved binning method

1 Introduction

The long-term density propagation problem is studied in many applications, such as the dynamic evolution of the interplanetary dust (Gor'kavyi et al. 1997a, b), nanosatellite constellations (McInnes 2000), swarms of high area-to-mass ratio spacecraft (Colombo and McInnes 2011), the global space debris population (Nazarenko 1997; Smirnov et al. 2001), small-debris-object clouds (Letizia et al. 2015, 2016a, b; Frey 2020), the asteroid post-encounter motion (Wittig et al. 2015), and clouds of high-altitude and high area-to-mass ratio satellites (Wittig et al. 2017; Sun et al. 2022a, b). To realize high-quality density propagation after long-term propagations, an accurate and efficient characterization for the highly nonlinear density is required.

Monte Carlo (MC) is a traditional method for density propagation. It provides reference density via a large number of random samples; however, is computationally intensive. To reduce the computational load, many nonlinear methods are developed for density propagation. In (Halder and Bhattacharya 2016), the authors classify the methods into two categories: parametric (where one evolves the statistical moments) and nonparametric (where one approximates or directly propagates the evolution equation of the Probability Density Function (PDF)). Representative nonparametric methods are Gaussian Mixture Model (GMM)-based hybrid methods (such as Gaussian Mixture Model-Unscented Transformation (GMM-UT) (Giza et al. 2009)), and Density Evolution Equation (DEE, or continuity equation) (McInnes 2000; Trisolini and Colombo 2021; Sun et al. 2022a). The former approximates the non-Gaussian PDF at any time using the weighted sum of the first two statistical moments of the Gaussians. The latter directly propagates the density as a fluid with continuous properties, and can be solved together with the propagation of the state space via the method of characteristics (Evans 1998; Halder and Bhattacharya 2016; Sun et al. 2022a). Since all the statistical moments can be derived from the PDF, with the nonparametric methods, we get all the density information at any time via the evolved PDF.

The DEE method has been developed over the years. Different from the MC method (where many simulations are conducted for an equivalent large number of random samples), we can get the density evolution of the entire clouds of objects through a finite number of simulations for a finite number of random samples, featuring a much lower computational load. The accuracy of the DEE method mainly depends on the dynamic nonlinearity, the performance of the interpolation method, and the binning method. In the work of (Sun et al. 2022a), the DEE method and the Gaussian mixture model are compared on the long-term phase space density propagation problem. It demonstrates the overall high accuracy of the DEE method for the long-term density propagation. However, when the phase space is highly deformed and elongated, the density accuracy of the case with fewer samples is low. This is because, when the density distribution is highly deformed and elongated, the actual density distribution is not convex. The Delaunay Triangulation-based Binning method adopted in the work of (Sun et al. 2022a) (we define it as the DT-B1 method in this paper) performs worse because it interpolates the density within the whole convex hull. The binning method in (Sun et al. 2022a) (i.e., the B1 method) calculates the joint and marginal density as the weighted mean of density weights per bin area and per bin width, respectively. In this case, the core value and the overall distribution characteristic of the joint density, and the peaks of the marginal density in two phase space directions, are underestimated.

Since the performance of the DEE method is mainly affected by the interpolation and the binning methods, to tackle the long-term density propagation problem featuring highly deformed and elongated density distribution, we will consider the following four aspects to improve the DEE method. First, an improved linear interpolation method based on the alpha shape triangulation (Trisolini and Colombo 2021) can be studied to get more accurate interpolated density by adapting to the evolution of the shape of the density space volume. Second, for the nonlinear dynamics under consideration, we should consider an improved binning method for accurate density calculation. The improved binning method should give weights to each bin for density calculation with the inclusion of the area weight, and the variant nonlinearity of the density within each alpha shape triangulation. Third, the problem of how many random samples are required for the DEE method for ensuring the density quality needs to be studied. In (Sun et al. 2022a), the smaller sample number case ($N_{sam} = 961$) cannot ensure the density accuracy for the DEE method, while the larger sample number case ($N_{sam} = 1E5$) is too computationally intensive. Fourth, the problem of how large the grid number *Ngrid* should be for performing the linear interpolation for ensuring the density quality and the computational efficiency needs to be studied. It should be noted that, for the highly deformed and elongated density distribution, the selected sample and grid number should be advantageous for selecting the DEE method for the long-term density propagation problem, i.e., with high density accuracy and computational efficiency compared with that of the MC method.

The motivation of this paper is to improve the density accuracy for the highly deformed and elongated density distribution within the continuum method framework using an improved Alpha shape Triangulation-based linear interpolation method, and an improved Binning method (defined as AT-B2). The improved Alpha shape Triangulation-based linear interpolation method (AT) is used to obtain linearly interpolated density within the actual non-convex hull enclosing all the samples. The improved Binning method (B2) calculates the joint and marginal density as the weighted sum of the density weights per bin area and per bin width, respectively. It increases the density accuracy by considering the weight for each alpha shape triangulation per bin area, and the variant nonlinearity of the density within each alpha shape triangulation. The suitable values of the sample number for the DEE method and the suitable grid number for performing the linear interpolation are selected by trading off the density accuracy and the computational effort. The Medium Earth Orbit (MEO) planar phase space case subject to the semi-analytical coupled effects of the solar radiation pressure and Earth's oblateness is given for demonstrating the improved performance in the density accuracy and the computational efficiency for the AT-B2 method.

The paper is organized as follows. Section 2 gives the problem statement. Section 3 presents the density evolution equation in nonlinear dynamics. In section 4, the improved alpha shape-based linear interpolation and binning method are presented, together with the whole computation procedure for solving the density propagation problem with the AT-B2 method, and the integrated illustration and comparison for DEE methods of DT-B1 and AT-B2. Section 5 presents the numerical simulations, including the simulation setup (defining the initial conditions for the MEO planar phase space case, the accuracy measure), density propagation results, and some discussion on the superiority of the AT-B2 method for accurate and efficient density propagation for the highly deformed and elongated density distribution. Section 6 gives some conclusions.

2 Problem statement

To achieve the long-term density propagation, we need to obtain the nonlinear density (i.e., the PDF) corresponding to the propagated state space after long-term propagations.

Given the following Ordinary Differential Equations (ODEs) governing the dynamic evolution, and the initial conditions in the state and density space,

$$\dot{\boldsymbol{x}}(t) = \boldsymbol{v}(\boldsymbol{x}(t), t), \ \boldsymbol{x}(t_0) = \boldsymbol{x}_0, \boldsymbol{p}_{t_0}(\boldsymbol{x}) \tag{1}$$

where $\boldsymbol{x}(t) \in \mathbb{R}^m$ is the state vector, m is the problem dimension, $\boldsymbol{v}:\mathbb{R}^m \rightarrow \mathbb{R}^m$ is the continuous acceleration terms for the nonlinear dynamics under consideration, $\boldsymbol{x}_0$ is the state space initial condition at time t_0, and $\boldsymbol{p}_{t_0}(\boldsymbol{x})$ is the initial PDF.

In this paper, we will focus on solving the long-term density propagation problem for the highly deformed and elongated density distribution within the continuum method framework, which directly propagates the evolution equation of the density to get the non-Gaussian PDF, $\boldsymbol{p}_t(\boldsymbol{x})$, at any time t, given the initial conditions in the state space $\boldsymbol{x}_0$ and the initial PDF $\boldsymbol{p}_{t_0}(\boldsymbol{x})$. Without loss of generality we will refer to density as the PDF for the remainder of this paper. It provides the probability of the object occupying an infinitely small state space volume around the state $\boldsymbol{x}$.

Different from the previous work, where the density accuracy of the case with fewer samples is low when the phase space is highly deformed and elongated, in this paper, we improve the density accuracy for the highly deformed and elongated density distribution using an improved alpha shape-based linear interpolation method, and an improved binning method. The suitable sample number for the continuum method and the suitable grid number for performing the linear interpolation are selected by trading off the density accuracy and the computational effort.

3 Density evolution equation

To study the density evolution within the continuum method framework, we need to propagate the density evolution equation together with the state space dynamics (see Eq. 1).

Assume that n is the density to be solved for the problem under consideration. Given m generic variables x_i, $i \in \{1,\cdots,m\}$, and assuming that the density is differentiable for all x_i, the density evolution equation is written as follows (Gor'kavyi et al. 1997a; McInnes 2000; Letizia et al. 2016a; Frey 2020; Sun et al. 2022a),

$$\frac{\partial n}{\partial t} + \frac{\partial n}{\partial x_1} v_1 + \cdots + \frac{\partial n}{\partial x_m} v_m + \left[\frac{\partial v_1}{\partial x_1} + \cdots + \frac{\partial v_m}{\partial x_m} \right] n = \dot{n}^+ - \dot{n}^- \tag{2}$$

where $\dot{n}^+ - \dot{n}^-$ is the discontinuous acceleration terms included for the dynamic system, such as the random on-orbit failure of existing nanosatellites on the topic of nanosatellite constellation evolution, v_i is the ith component of the continuous acceleration terms $\boldsymbol{v}(\boldsymbol{x}(t), t)$ (see Eq. 1). In this paper, no discontinuous acceleration terms are considered, i.e., $\dot{n}^+ - \dot{n}^- = 0$. By applying the method of characteristics (Evans 1998), the following equations are obtained (Letizia et al. 2016a),

$$\begin{cases} \dfrac{dt}{du} = 1 \\ \dfrac{dx_1}{du} = v_1(x_1, \cdots, x_m) \\ \vdots \\ \dfrac{dx_m}{du} = v_m(x_1, \cdots, x_m) \\ \dfrac{dn}{du} = -\left[\dfrac{\partial v_1}{\partial x_1} + \cdots + \dfrac{\partial v_m}{\partial x_m}\right] n(x_1, \cdots, x_m, t) \end{cases} \tag{3}$$

where u is a parametrisation of the characteristic lines. From Eq. (3), we can see that given the specific formulation for the dynamic system (i.e., given the actual expressions of v_i), the time evolution of the density $n(x_1, \cdots, x_m, t)$ can be obtained together with the state space variables x_i.

To obtain the propagated density (i.e., the non-Gaussian PDF, $\boldsymbol{p}_t(\boldsymbol{x})$) for the DEE method at any time t, the following three steps are required. First, generate initial random samples with a predefined sample number N_{sam} subject to the given initial PDF $\boldsymbol{p}_{t_0}(\boldsymbol{x})$, and calculate the initial density weights $n(x_1, \cdots, x_m, t_0)$ for the samples at time t_0. Thus, initial samples in the m-dimensional state space $(x_1, \cdots, x_m)$ and their associated density weights are obtained in the $(m + 1)$-dimensional extended state space $(x_1, \cdots, x_m, n)$. Note that the selection of the sample number N_{sam} is important, because it influences the density accuracy and the whole computation time. Second, integrate the density evolution equation together with the state space dynamics (see Eq. 3) to obtain the propagated samples and the associated density weights in the $(m + 1)$-dimensional extended state space. Third, calculate the density by processing the final samples and density weights in a statistical way. In this paper, the linear interpolation method is combined with the binning method to calculate the density.

4 Improved alpha shape-based interpolation and binning method

To improve the density accuracy within the continuum method framework for the highly deformed and elongated density distribution, we present an improved alpha shape-based linear interpolation method, and an improved binning method, identified with AT-B2, for the accurate and efficient long-term density propagation. In this section, we first introduce the improved alpha shape-based linear interpolation method and the improved binning method, respectively. Then, we present the whole procedure for solving the density propagation problem with the AT-B2 method, and the integrated illustration and comparison for DEE methods of DT-B1 and AT-B2.

4.1 Improved alpha shape-based linear interpolation method

For the highly deformed and elongated density distribution, in this paper, we include the concept of alpha shape to get accurate interpolated density within the non-convex hull enclosing all the samples. Different from the DT method, which is done within the whole convex hull of the scattered sample data, the AT method helps adapt to the evolution of the shape of the state space volume.

Assume a generic 2D problem defined in two independent variables $x_i, i \in \{1,2\}$, the N_{sam} propagated samples and their associated density weights at any time t in the vectors $(x_{10},$

$x_{20}, n_0(x_{10}, x_{20}, t)$), and the grid number *Ngrid* for each dimension for conducting the linear interpolation. To get the alpha shape triangulation-based interpolated density, three steps are required. First, perform the Delaunay triangulation-based interpolation for the specified query points (x_1, x_2) (Trisolini and Colombo 2021),

$$n(x_1, x_2, t) = \sum_{i=1}^{V} n_i B_i(x_1, x_2) \tag{4}$$

where $n(x_1, x_2, t)$ is the Delaunay triangulation-based linear interpolated density of the point (x_1, x_2), V is the number of vertices of the simplex for the Delaunay triangulation, n_i is the value of the density for the ith vertex, $B_i(x_1, x_2)$ is the barycentric coordinates of the ith vertex including the point (x_1, x_2). As we can see in Eq. (4), if we find the barycentric coordinates of the vertices, the linear interpolation can be done. The main advantage of the DT method is the capability of retaining the scattered samples at the nodes of the triangulation (Preparata and Shamos 1985). Theoretically, the larger the sample number N_{sam}, the better the density quality for the DT method. Second, generate the compact alpha shape triangulation within the actual non-convex hull enclosing all the scattered sample data for a predefined alpha radius r_a (Edelsbrunner and Mücke 1994; Trisolini and Colombo 2021),

$$As = \{A_i(x_{10}, x_{20}, r_a),\ i \in \{1, 2, \cdots, V_A\} | A_i \subseteq D(x_{10}, x_{20})\} \tag{5}$$

where As is the generated alpha shape triangulation, A_i is the ith vertex of the simplex for the alpha shape triangulation, V_A is the number of vertices of the simplex for the alpha shape triangulation, $D(x_{10}, x_{20})$ is the Delaunay triangulation for the samples (x_{10}, x_{20}). As we can see in Eq. (5), the generated alpha shape triangulation is the subset of the Delaunay triangulation. The alpha shape is introduced to remove the surplus vertices of the simplex generated when the shape of the density distribution is not convex. Note that the selection of the alpha radius r_a is important, as it decides how accurate the alpha shape triangulation characterizes the actual shape of the density distribution. In this paper, we check different r_a values using the dichotomy, and determine the most appropriate for the test cases in examination. To further improve the density accuracy while still granting an improved computational efficiency, the adaptive determination of the suitable value of the alpha radius for each case needs to be given into an insight in future work. In principle, also in this case, the larger the sample number N_{sam}, the better the returned alpha shape triangulation is at characterizing the evolved shape of the density space. Third, retain all the Delaunay triangulation-based interpolated results that are inside or make up the alpha shape triangulation, and perform the alpha shape triangulation-based linear interpolation (Trisolini and Colombo 2021),

$$n_a(x_1, x_2, t) = \sum_{i=1}^{V_A} n_{ai} B_{ai}(x_1, x_2) \tag{6}$$

where $n_a(x_1, x_2, t)$ is the alpha shape triangulation-based linear interpolated density of the point (x_1, x_2), n_{ai} is the value of the density for the ith vertex for the alpha shape triangulation, $B_{ai}(x_1, x_2)$ is the barycentric coordinates of the ith vertex including the point (x_1, x_2) for the alpha shape triangulation.

With the above three steps, we get the improved alpha shape-based linearly interpolated density by retaining the Delaunay triangulation-based interpolated results within the alpha shape triangulation. Note that, the selection of the sample number N_{sam} and the grid number *Ngrid* is important, because it affects the accuracy of the final interpolated density $n_a(x_{1a}, x_{2a}, t)$, and the computational efficiency. In this paper, we will select the suitable sample number

N_{sam} and the grid number $Ngrid$ by trading off the density accuracy and computational efficiency.

4.2 Improved binning method

With the interpolated results in the vectors $(x_1, x_2, n_a(x_1, x_2, t))$ at time t, an improved binning method is presented in this paper for density calculation. Different from the B1 method (which calculates the joint and marginal density as the weighted mean of density weights per bin area and per bin width, respectively), the B2 method calculates the joint and marginal density as the weighted sum of density weights per bin area and per bin width, respectively. In Sect. 5, we will show that this method increases the density accuracy by considering the weight for each alpha shape triangulation per bin area, and the variant nonlinearity of the density within each alpha shape triangulation.

To get the joint and marginal density for the B2 method, three steps are required. First, partition the density weights $n_a(x_1, x_2, t)$ into the 2D uniformly divided bins in the vectors (x_1, x_2). Second, with the defined 2D bins, calculate the joint density as the weighted sum of density weights per bin area, as follows,

$$f_{DEE-pk}(x_1, x_2, t) = \frac{S_{pk}/A_{pk}}{\sum_{p=1}^{B_x}\sum_{k=1}^{B_y} S_{pk}} \tag{7}$$

where S_{pk} is the sum of the density weights $n_a(x_1, x_2, t)$ in each bin, $p \in \{1, \cdots, B_x\}$, $k \in \{1, \cdots, B_y\}$, B_x and B_y are the defined bin number for the two state space directions, respectively, A_{pk} is the area of each bin. Third, calculate the marginal density for each direction by integrating the joint density throughout the whole domain of the other direction. Here we present the equation for the marginal density for the first dimension,

$$f_{DEE-1}(x_1, t) = \sum_{L_2}^{U_2} f_{DEE-pk}(x_1, x_2, t) dx_2 \tag{8}$$

where L_2 and U_2 are the lower and upper bounds of the bin edges for the second dimension, respectively.

4.3 Density propagation with the AT-B2 method

In this section, we first present the whole procedure for solving the density propagation problem with the AT-B2 method presented in this paper, which combines an improved alpha shape-based linear interpolation method, and an improved binning method for accurate density calculation. Then, the integrated illustration and comparison for DEE methods of AT-B2, DT-B1, AT-B1 is given. Note that the AT-B1 method is the combination of the AT method and the B1 method for density propagation. It is given in this paper as a baseline method to demonstrate the superiority of the AT method and the B2 method, respectively, for the AT-B2 method, compared with the DT-B1 method. Also note that to make sure of the density quality with a low computational effort, in this paper, we select the suitable sample number N_{sam} for dynamic propagation and the suitable grid number $Ngrid$ for performing the linear interpolation via the trade-off between the density accuracy and the computational efficiency.

The computation procedure for solving the density propagation problem with the AT-B2 method is given in Table 1. Table 2 shows the combinations of options for DEE methods of

Table 1 Computation procedure for solving the density propagation problem with the AT-B2 method

Step	Content
1	Determine initial conditions: 1. Formulate the dynamics for the state space and the density evolution (Eqs. 1 and 3) 2. Give the density propagation time t 3. Select a predefined alpha radius r_a for generating a compact alpha shape triangulation enclosing all the samples
2	Select the sample number N_{sam} and the grid number $Ngrid$ by trading off the accuracy and efficiency
3	Conduct improved alpha shape triangulation-based linear interpolation for propagated samples (Eqs. 4–6)
4	Conduct improved binning method for the interpolated density for density calculation (Eqs. 7–8);

Table 2 Comparison for DEE methods

DEE method	DT-B1	AT-B1	AT-B2
Linear interpolation method	DT	AT	AT
Binning method	B1	B1	B2

DT-B1, AT-B1 and AT-B2, in terms of the composition of the linear interpolation method and the binning method. Figure 1 shows the illustration and comparison for the DT and AT methods for the case DEE-961 for Scenario 1, $t = 1$ yr in the work of (Sun et al. 2022a), where the red solid points are the $N_{sam} = 961$ propagated samples in the solar angle-eccentricity (ϕ, e) 2D phase space (see Figs. 3, 4 in Sun et al. 2022a). As we can see from Fig. 1, for the highly deformed and elongated density distribution, for the DT method, gray interpolated points are generated within the whole convex hull of the scattered sample data. For the AT method, the compact alpha shape triangulation enclosing all the samples is generated for a predefined alpha radius $r_a = 2$. Figure 1b gives the snapshot around the point (ϕ, e) = (π, 0.804) for the AT method. From Fig. 1b, we can see that the AT method is done by

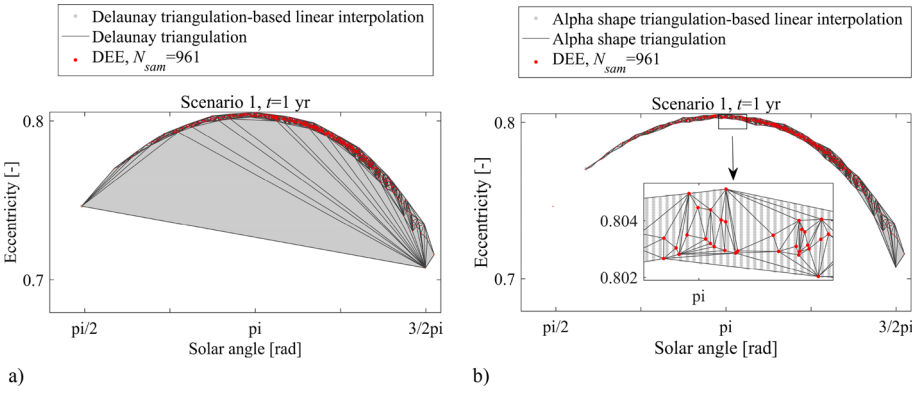

Fig. 1 Illustration and comparison for the (**a**) DT and (**b**) AT methods for Scenario 1, $t = 1$ yr ($N_{sam} = 961$)

retaining all the Delaunay triangulation-based linearly interpolated results within the alpha shape triangulation, which adapts to the shape of the density space volume.

5 Numerical simulations

The novelty of this paper is to improve the density accuracy for the highly deformed and elongated density distribution within the continuum method framework using an improved alpha shape triangulation-based linear interpolation method, and an improved binning method.

In this paper, the MEO planar phase space case is chosen to give an insight into the long-term density propagation problem in the context of high-altitude and high area-to-mass ratio satellite long-term propagation (Krivov and Getino 1997; Wittig et al. 2017; Sun et al. 2022a, b). The test cases are the same of the previous paper (Sun et al. 2022a). It should be noted that in this paper, the high-altitude refers to the higher orbital altitude ($2R_E \leq a \leq 3R_E$, where a is the semimajor axis, R_E is the equatorial radius of Earth) in the MEO region.

In this section, we will give the simulation setup (defining the initial conditions for the MEO planar phase space case, and the accuracy measure for the DEE methods), the density results for the test cases of Scenario 1, $t = 1$ yr, and Scenario 2, $t = \{1.5, 3\}$ yrs (see the results for Scenario 2 in "Appendices"), and some discussion on the superiority of the AT-B2 method for the long-term density propagation in terms of the density accuracy and the computational efficiency. Note that the three cases are chosen from the work of (Sun et al. 2022a). They are used to demonstrate the improved density quality for the highly deformed and elongated density distribution within the continuum method framework.

5.1 Simulation setup

5.1.1 Definition of the initial conditions for the MEO planar phase space case

The evolution equation of the dynamic system subject to the semi-analyzed coupled effect of the Earth's oblateness and the solar radiation pressure is (Krivov and Getino 1997)

$$\dot{\boldsymbol{x}}(t) = \boldsymbol{v}(\boldsymbol{x}(t),\, t) = \begin{bmatrix} v_1(\boldsymbol{x}(t),\, t) \\ v_2(\boldsymbol{x}(t),\, t) \end{bmatrix} = \begin{bmatrix} n_s\left(C\sqrt{1-e^2}\sin\phi\right) \\ n_s\left(C\dfrac{\sqrt{1-e^2}}{e}\cos\phi + \dfrac{W}{\left(1-e^2\right)^2} - 1\right) \end{bmatrix} \tag{9}$$

where $\boldsymbol{x} = [e; \phi]$ (eccentricity; solar angle) is the state vector to describe the planar equatorial orbit, n_s is the mean motion of the sun, and C and W represent the dimensionless radiative and oblateness parameters, respectively. Here we assume $C = 0.15$, $W = 0.409$, and $a = 2.5\ R_E$, corresponding to the phase portrait of type III in Fig. 1 in (Sun et al. 2022a). Here a is treated as constant as no eclipses are considered in this paper. Figure 2 shows the phase portrait and the divided phase space domains in Fig. 1 in (Sun et al. 2022a). The horizontal line marks the critical eccentricity $e_{cri} = 0.6$ for Earth reentry at the Earth surface. In this phase portrait, phase space bifurcation is detected at the stationary point P_4. The Hamiltonian phase space is divided into three sub-domains $SubD_i$, $i \in \{1,2,3\}$, departed by the contour lines passing by the stationary points P_1 and P_4. To get the density together with the state space, the density evolution equation of the dynamic system is calculated as

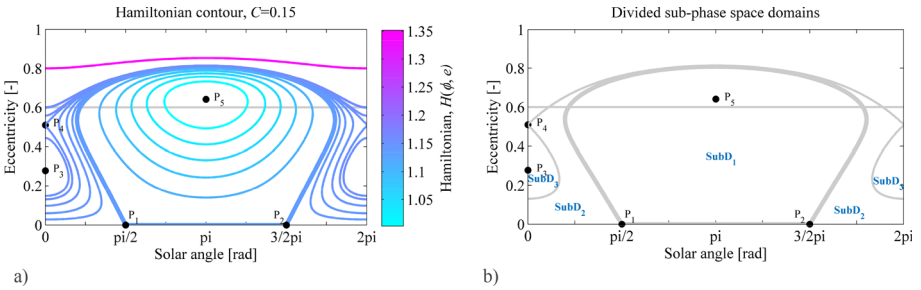

Fig. 2 (**a**) Phase portrait of type III; (**b**) Divided sub-phase space domains ($a = 2.5\ R_E$, $W = 0.409$, $C = 0.15$, critical eccentricity $e_{cri} = 0.6$ for Earth reentry; Sun et al. 2022a)

Table 3 Initial multivariate Gaussian uncertainty distribution for the three test cases

Scenario	mean, $\boldsymbol{m}_0$ [rad; -]	Covariance matrix, $\boldsymbol{P}_0$	t, [yr]
1	$[\phi_0; e_0]$=[2.2069; 0.145]	diag{0.0386, 6.25E-4}	1
2	$[\phi_0; e_0]$=[0.5419; 0.095]	diag{0.0015, 2.5E-5}	1.5 3

$$\frac{dn}{dt} = -\left(\frac{\partial}{\partial e}\left(\frac{de}{dt}\right) + \frac{\partial}{\partial \phi}\left(\frac{d\phi}{dt}\right)\right)n = \frac{C \cdot n_s \cdot \sin\phi}{e\sqrt{1-e^2}}n \tag{10}$$

Table 3 gives the initial conditions in terms of the mean $\boldsymbol{m}_0$ and covariance matrix $\boldsymbol{P}_0$ of the initial Gaussian distribution, and the propagation time t for the three test cases. It should be noted that, for the first test case (i.e., Scenario 1, $t = 1$ yr), it is defined to ensure the realization of the long-term density propagation within the sub-phase space domain SubD_1 (see Fig. 2). For the other two test cases (i.e., Scenario 2, $t = \{1.5, 3\}$ yrs), they are defined to ensure the realization of the long-term density propagation within the sub-phase space domain SubD_2 (see Fig. 2), featuring the same initial Gaussian distribution, but differing in the propagation time t.

To complement the accuracy and efficiency analysis for DEE methods with respect to that of MC, a MC simulation is performed for the three test cases. The number of MC samples is set to be $N_{sam} = 1\text{E}5$ for ensuring the convergence of the MC method and avoiding a higher computational load for a test case with a larger sample number.

To give a better choice of the sample number N_{sam} and the grid number $Ngrid$ for the DEE methods, the sample number N_{sam} is chosen within the parameter set, $N_{sam} \in \{500,961,1000,2000,4000,8000,16000,32000,64000,1\text{E}5\}$, and the grid number $Ngrid$ is chosen within the parameter set, $Ngrid \in \{500,1000,1500,2000,2500,3000\}$. Table 4 summarizes the predefined parameter sets of N_{sam} and $Ngrid$ for DEE methods. The two parameter

Table 4 Predefined parameter sets of the sample number N_{sam} and the grid number $Ngrid$ for DEE methods

Variable	N_{sam}	$Ngrid$
Predefined parameter set	{500,961,1000,2000,4000,8000,16000, 32000,64000,1E5}	{500,1000,1500,2000,2500,3000}

sets are defined in this paper for the following considerations. For the parameter set of the sample number N_{sam}, it is set to be exponentially distributed except the two elements {961, 1E5}, which are the reference sample number for the cases of DEE-961 and DEE-1E5 in the work of (Sun et al. 2022a). In (Sun et al. 2022a), we can see that, for the case with more samples (i.e., DEE-1E5), the high density accuracy level comparable with that of the MC method can be achieved, but with a computational effort larger than that of the MC method. For the case with fewer samples (i.e., DEE-961), when the phase space is highly deformed and elongated, the density accuracy level is low. Thus, within this parameter domain [500, 1E5] for the sample number, the evolution characteristic for the density accuracy and the computational efficiency with respect to the N_{sam} can be preliminarily exploited. For the parameter set of the grid number *Ngrid*, it is set to be linearly distributed. As we can infer in (Sun et al. 2022a), only when the number of the propagated density samples is large enough for characterizing the deformed and elongated density distribution, accurate density can be calculated via the linear interpolation and the binning method. Thus, for the contribution of the density accuracy and the computational efficiency, the value of the sample number N_{sam} may weigh much more than the grid number *Ngrid* in affecting the accuracy and the efficiency for the DEE method. Within the domain [500, 3000] for the grid number, the evolution characteristic for the density accuracy and the computational efficiency with respect to the *Ngrid* can be preliminarily exploited.

5.1.2 Definition of the accuracy measure

To determine the density accuracy for DEE methods with respect to that of MC, in this paper, the Likelihood Deviation (LD) is used to be the accuracy measure as follows (Sun et al. 2022b),

$$\mathrm{LD} = \frac{\sqrt{\sum_{i=1}^{N} \left(f_{\mathrm{DEE}}(\boldsymbol{x}_j) - q(\boldsymbol{x}_j)\right)^2}}{N} \tag{11}$$

where N is the number of MC samples, $\boldsymbol{x}_j$ is the jth MC sample, $f_{\mathrm{DEE}}(\boldsymbol{x}_j)$ is the density of the jth MC sample for the DEE methods, $q(\boldsymbol{x}_j)$ is the density of the jth MC sample for the MC method. The LD measure quantifies the density accuracy for the DEE methods compared with that of the MC method. The smaller the LD measure, the higher density accuracy for the DEE methods compared with that of the MC method.

For the case in examination, to evaluate the overall accuracy level for DEE methods with respect to that of the MC method, the following performance index J_p is predefined as the weighted sum of the LD measure for the density,

$$J_p = w_d \cdot \sum \mathrm{LD} \tag{12}$$

where w_d is the density weight, ΣLD is the sum of the LD measure for the joint and marginal density. In this paper, we assume the same weight $w_d = 1/3$ for the joint and marginal density for the 2D problem. The smaller the performance index J_p, the higher overall accuracy level for the DEE method compared with that of the MC method.

5.2 Results

In this section, results will be given in the two sections as follows. Section 5.2.1 gives the selected sample number N_{sam} and the grid number *Ngrid* by trading off the density accuracy

and the computational efficiency for the DEE methods. Section 5.2.2 presents the density results for the DT-B1, AT-B1, and AT-B2 methods compared with that of the MC method. Note that for the test case Scenario 1, $t = 1$ yr, results are shown in the text. For the other two cases of Scenario 2, $t = \{1.5, 3\}$ yrs, results are shown in the "Appendices".

5.2.1 Selection of the sample number N_{sam} and grid number *Ngrid* (Scenario 1, $t = 1$ yr)

To select the better value of the sample number N_{sam} and the grid number *Ngrid* for the DEE methods of DT-B1, AT-B1 and AT-B2, we perform the accuracy and the efficiency analysis with respect to that of the MC method for the predefined parameter sets of the sample number and the grid number (see Table 4). The density accuracy is evaluated via the LD measure and the performance index J_p (see Eqs. 11, 12). The computational efficiency is evaluated via the normalized computational effort with respect to that of the MC method.

For the case Scenario 1, $t = 1$ yr, the values of the sample number and the grid number are selected as $N_{sam} = 4000$, $Ngrid = 1000$ for the AT-B2 method. Figure 3 presents the evolution of the normalized LD measure for the joint and marginal density with N_{sam}, and with *Ngrid*, respectively, for AT-B2, AT-B1 and DT-B1 methods, with respect to the case AT-B2 ($N_{sam} = 4000$, $Ngrid = 1000$). The smaller the normalized LD measure for a specific N_{sam}/*Ngrid* case, the higher accuracy for the density for the specific case with respect to the selected case AT-B2 ($N_{sam} = 4000$, $Ngrid = 1000$). Note that, to perform the density accuracy analysis for the DEE methods with respect to that of the MC method (via the LD measure and the predefined performance index), for the case in examination, B_x and B_y are given as the bin numbers for the solar angle and the eccentricity direction, respectively, for the joint density calculation, for all the DEE methods. The grid number *Ngrid* gives the bin number for two phase space directions for performing the linear interpolation for all the DEE methods and represents the bin number for two directions for the marginal density calculation. Figure 4 gives the evolution of the normalized performance index with N_{sam}, and

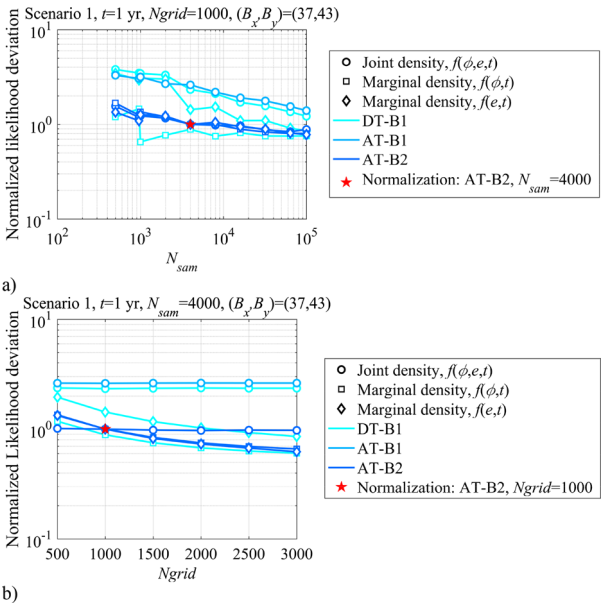

Fig. 3 Normalized LD evolution (**a**) with N_{sam}, and (**b**) with *Ngrid*, for DEE methods, with respect to the case AT-B2 ($N_{sam} = 4000$, $Ngrid = 1000$), for Scenario 1, $t = 1$ yr

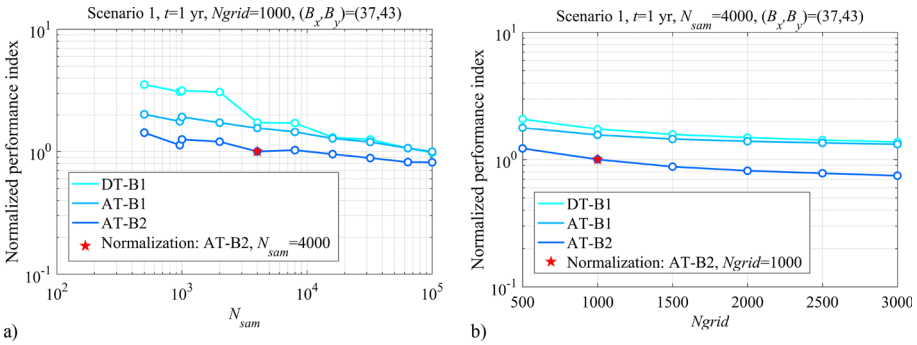

Fig. 4 Normalized performance index J_p evolution (**a**) with N_{sam}, and (**b**) with $Ngrid$, for DEE methods, with respect to the case AT-B2 ($N_{sam} = 4000$, $Ngrid = 1000$), for Scenario 1, $t = 1$ yr

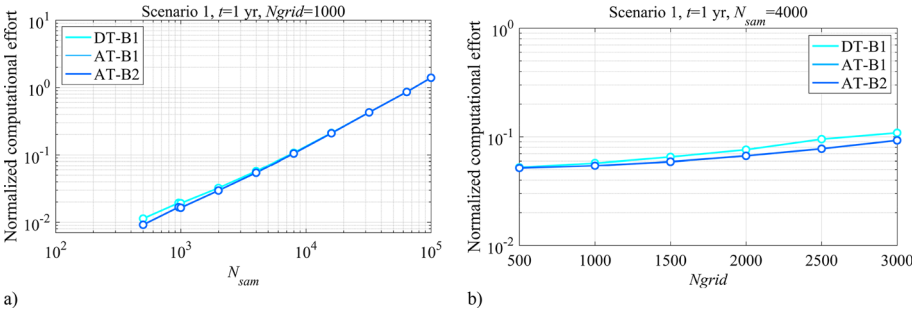

Fig. 5 Normalized computational effort evolution (**a**) with N_{sam}, and (**b**) with $Ngrid$, for DEE methods, with respect to the MC method, for Scenario 1, $t = 1$ yr

with $Ngrid$, respectively, with respect to the case AT-B2 ($N_{sam} = 4000$, $Ngrid = 1000$). The smaller the normalized performance index, the higher overall accuracy level for the specific case with respect to the selected case AT-B2 ($N_{sam} = 4000$, $Ngrid = 1000$). Figure 5 presents the evolution of the normalized computational effort with N_{sam}, and with $Ngrid$, respectively, with respect to that of the MC method.

Here we present the procedures for the determination of the sample number $N_{sam} = 4000$ for the AT-B2 method by trading off the density accuracy and the computational efficiency. First, as we can see from Fig. 3a, the smallest LD measure (i.e., the highest density accuracy) for the joint density and the marginal density of the eccentricity is obtained for the AT-B2 method. Overall, for the AT-B2 and AT-B1 methods, the LD measure of the joint and marginal density drops consistently with the increase in the sample number N_{sam}, indicating a higher density accuracy stability with respect to the sample number N_{sam}. Interestingly, though the highest LD measure (i.e., the lowest density accuracy) is obtained for the DT-B1 method for the joint density and the marginal density of the eccentricity, overall, it outperforms the AT-B1 and AT-B2 methods in capturing the marginal density of the solar angle, except the case AT-B2 ($N_{sam} = 961$). Similarly, for the AT-B1 method, it outperforms the DT-B1 method in capturing the joint density and the marginal density of the eccentricity, but not in capturing the marginal density of the solar angle. This means that for the DT-B1 and AT-B1 methods, they fail to get the higher accuracy for both the joint and marginal density. For the sample number $N_{sam} \geq 4000$, little discrepancy is shown for the LD measure for the marginal density of the solar angle for the AT-B2 and DT-B1 methods (i.e., indicating the comparable

high accuracy level for the two methods). Second, as we can see from Fig. 4a, overall, for the AT-B2, AT-B1 and DT-B1 methods, the larger the sample number N_{sam}, the smaller the performance index (i.e., the higher accuracy level). The method accuracy ranking AT-B2>AT-B1>DT-B1 is obtained. This is not unexpected, because for the AT-B2 and AT-B1 methods, the linear interpolation is done within the compact non-convex polygon enclosing all the samples (see Fig. 1). This neglects many Delaunay triangulation-based interpolated points outside the alpha shape triangulation. In this case, the overall weights for the interpolated points within the alpha shape triangulation for the AT method are increased compared with that for the DT method, and thus the higher accuracy in capturing the core values and the distribution characteristics of the joint and marginal density. Also note that, for the AT-B2 method, the joint density is calculated using the weighted sum of the density weights per bin area, which allows for the variant nonlinearity of the density within each alpha shape triangulation. For the sample number $N_{sam} \geq 4000$, little changing amplitude is shown for the evolution of the performance index for the AT-B2 method, indicating the high stability for the overall density accuracy level ranking. Third, from Fig. 5a, we can see that the normalized computational effort evolves exponentially with the sample number N_{sam}, for AT-B2, AT-B1 and DT-B1 methods (note that, here in Fig. 5, the coordinates for the two phase space directions are plotted using a log scale). The method efficiency ranking {AT-B2, AT-B1}>DT-B1 is obtained. Overall, little difference is shown for the normalized computational effort for the three DEE methods. This is because the main difference among the three DEE methods is the post-processing for the propagated samples using the different linear interpolation and the binning methods. For the AT-B2 and AT-B1 methods, less interpolated points (within the compact alpha shape triangulation) are processed than that for the DT-B1 method (within the whole convex hull) for density calculation. With the increase in the sample number, i.e., for $N_{sam} \geq 4000$, the computational effort part of the dynamical propagation of the samples makes up the main part of the total computational effort, compared with the computational effort part of the density calculation using the linear interpolation and the binning methods, leading to the overall little difference for the normalized computational effort for the AT-B2, AT-B1, DT-B1 methods. For the case Scenario 1, $t = 1$ yr, the computation time for the MC method is 621.92 s. For the AT-B2 method, for the case $N_{sam} = 4000$, the normalized computational effort accounts for only 5.43% of that of the MC method. From Fig. 5a, we can infer that, for the AT-B2 method, to ensure a computational effort no larger than 20.92% of that of the MC method, the sample number should not be larger than $N_{sam} = 1.6E4$. Based on the above three-aspect analysis, the sample number $N_{sam} = 4000$ is selected for the AT-B2 method for the highly accurate density, and the high computational efficiency.

Through a similar procedure, as we can see from Figs 3b, 4b and 5b, the better value of the grid number $Ngrid = 1000$ can be selected for the AT-B2 method.

For the AT-B2 method, as we can see from Figs. 3, 4, 5, larger changing amplitudes in terms of the normalized LD measure (see Figs. 3a, b), the normalized performance index (see Figs. 4a, b), and the normalized computational effort (see Figs. 5a, b), are obtained with respect to the sample number N_{sam} than the grid number $Ngrid$. This means that the sample number N_{sam} plays a more important role than the grid number $Ngrid$ in affecting the density accuracy and the computational efficiency. It is not unexpected, since only when the sample number N_{sam} is large enough for characterizing the highly nonlinear density distribution, accurate density can be calculated via the linear interpolation and the binning method for a selected grid number $Ngrid$. For the DEE methods, the main computation effort lies in the dynamical propagation part for propagating the N_{sam} samples. Note that, no apparent change appears for the LD measure for the joint density with the evolution of the grid number $Ngrid$, while the LD measure of the marginal density drops with the increase in the grid

number *Ngrid* (Fig. 3b). This means, for the case in examination, the selection of the grid number *Ngrid* mainly affects the accuracy of the marginal density, but not the joint density. Overall, we can conclude that the AT-B2 method outperforms the AT-B1 and DT-B1 methods for the long-term density propagation featuring the highly deformed and elongated density distribution in terms of the density accuracy and the computational efficiency.

5.2.2 Density results (scenario 1, $t = 1$ yr)

For the selected sample number and the grid number $\{N_{sam} = 4000, Ngrid = 1000\}$ for the case Scenario 1, $t = 1$ yr, now we present the joint and marginal density in Figs. 6 and 7, for the AT-B2 method compared with the AT-B1, DT-B1 methods with respect to that of the MC method. Note that, to highlight the heavier significance of the sample number than the grid number in affecting the density accuracy for the DEE methods, in Figs. 6 and 7, we present also the density for a smaller sample number case with $\{N_{sam} = 961, Ngrid = 1000\}$, which is exactly the case DEE-961 in the work of (Sun et al. 2022a). Thus, a parallel comparison of the improved results in this paper compared with that in (Sun et al. 2022a) can also be done.

From Figs. 6c, e and g, we can see that, for the selected cases with $\{N_{sam} = 4000, Ngrid = 1000\}$ for the AT-B2, AT-B1 and DT-B1 methods, the higher accuracy in the joint density is obtained with respect to that of the MC method (see Fig. 6a) compared with that for the smaller sample number cases with $\{N_{sam} = 961, Ngrid = 1000\}$(see Figs. 6b, d and f). The highest accuracy in the joint density is obtained for the AT-B2 method (see Fig. 6g). Little discrepancy is shown in the joint density accuracy for the AT-B2 method than that for the AT-B1 and DT-B1 methods when increasing the sample number from $N_{sam} = 961$ to $N_{sam} = 1E5$, indicating the higher stability for the density accuracy with respect to the sample number N_{sam} for the AT-B2 method (for the AT-B2 method, see Figs. 6f, g; for the AT-B1 method, see Figs. 6d, e; for the DT-B1 method, see Figs. 6b, c). This is consistent with the aforementioned results in Figs. 3a and 4a. Similarly, for the marginal density of the solar angle, we can conclude that for the selected cases with $\{N_{sam} = 4000, Ngrid = 1000\}$ for the AT-B2, AT-B1 and DT-B1 methods, the higher accuracy is obtained with respect to that of the MC method (see Fig. 7b), compared with that for the smaller sample number cases with $\{N_{sam} = 961, Ngrid = 1000\}$ (see Fig. 7a). For the marginal density of the solar angle and the eccentricity, the highest accuracy is obtained for the AT-B2 method (see Figs. 7b, d).

5.3 Discussion

For the case Scenario 1, $t = 1$ yr, the highest accuracy in terms of the joint and marginal density is obtained for the AT-B2 method for the selected case with $\{N_{sam} = 4000, Ngrid = 1000\}$. Overall, the AT-B2 method outperforms the DT-B1 and AT-B1 methods in capturing the core value and the distribution characteristic of the joint density, and the peak values and the distribution characteristics of the marginal density of the solar angle and the eccentricity (for the case Scenario 1, $t = 1$ yr, see Figs. 6g, 7b and d; for the cases Scenario 2, $t = \{1.5, 3\}$ yrs, see the "Appendices").

The advantages of the AT-B2 method are shown in the higher density accuracy (see Fig. 3a), the higher stability for the density accuracy with respect to the sample number N_{sam} and the grid number *Ngrid* (see Figs. 4a, b), and the higher computational efficiency compared with that of the MC method (see Figs. 5a, b). The sample number N_{sam} plays a more important role than the grid number *Ngrid* in affecting the density accuracy and the computational efficiency for the DEE methods. For the planar phase space long-term density

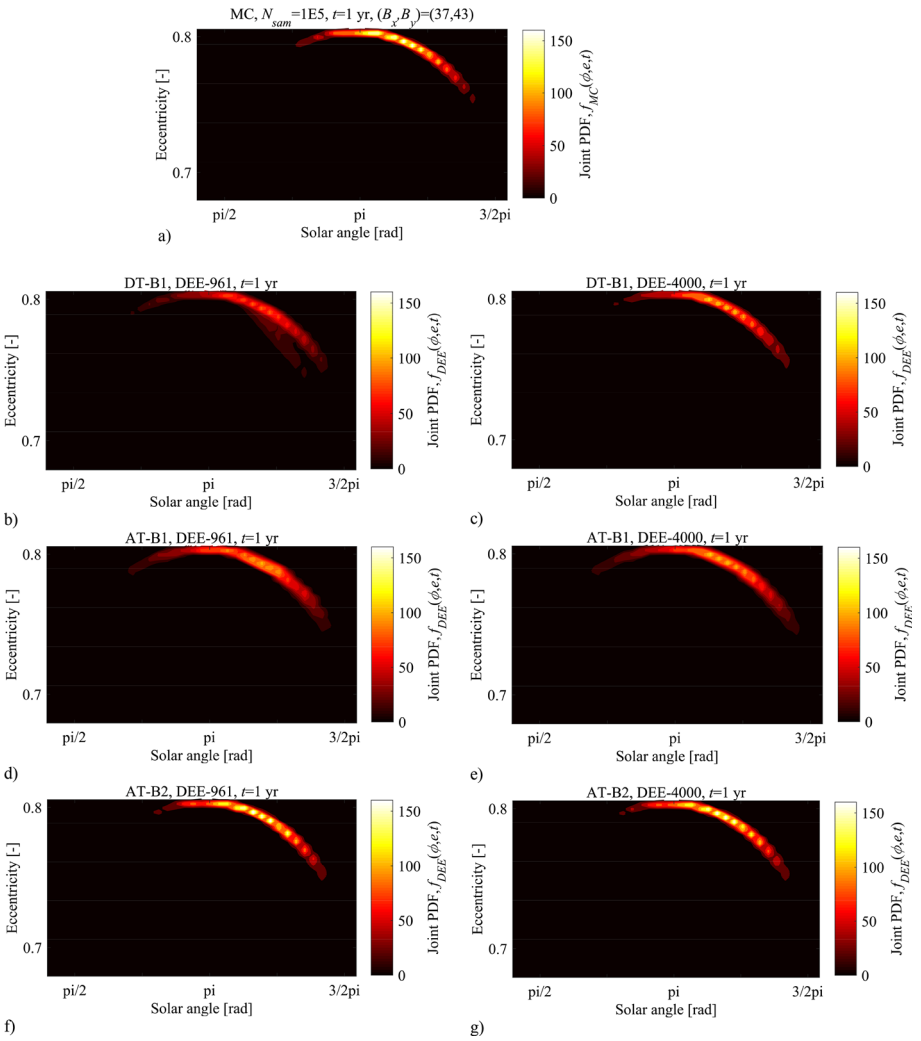

Fig. 6 The joint density (**a**) for the MC method; for the DT-B1 method, with (**b**) $\{N_{sam} = 961, Ngrid = 1000\}$, (**c**) $\{N_{sam} = 4000, Ngrid = 1000\}$; for the AT-B1 method, with (**d**) $\{N_{sam} = 961, Ngrid = 1000\}$, (**e**) $\{N_{sam} = 4000, Ngrid = 1000\}$; for the AT-B2 method, with (**f**) $\{N_{sam} = 961, Ngrid = 1000\}$, (**g**) $\{N_{sam} = 4000, Ngrid = 1000\}$ (for Scenario 1, $t = 1$ yr)

propagation problem featuring the highly deformed and elongated density distribution, the combination of the improved alpha shape-based linear interpolation method and the improved binning method (presented in Sect. 4 in this paper) is necessary for the accurate and efficient density propagation.

6 Conclusion

This paper presents an improved method within the continuum method framework by combining the improved alpha shape-based linear interpolation method and the improved binning

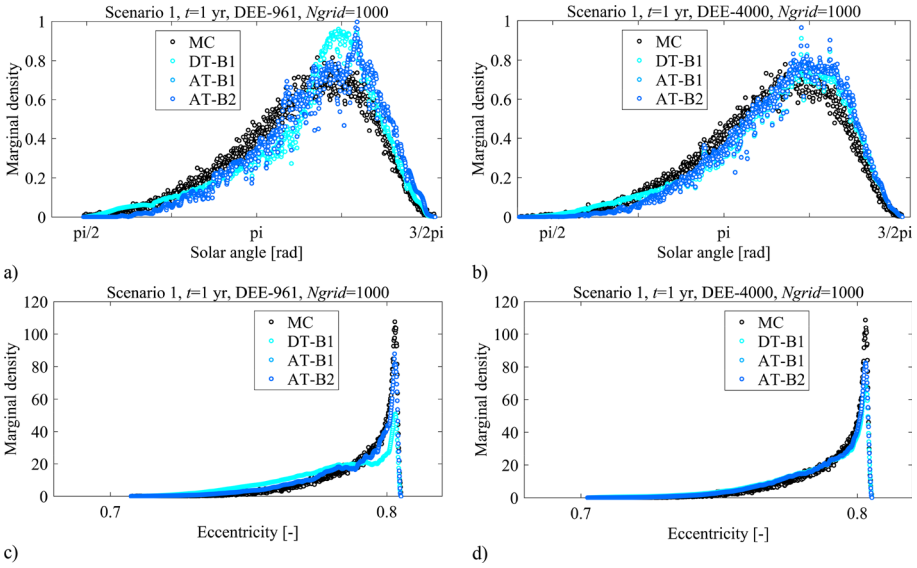

Fig. 7 The marginal density of the solar angle with (**a**) $\{N_{sam} = 961, Ngrid = 1000\}$, (**b**) $\{N_{sam} = 4000, Ngrid = 1000\}$, and the marginal density of the eccentricity with (**c**) $\{N_{sam} = 961, Ngrid = 1000\}$, (**d**) $\{N_{sam} = 4000, Ngrid = 1000\}$, for DT-B1, AT-B1 and AT-B2 methods with respect to the MC method, for Scenario 1, $t = 1$ yr

method, for the accurate and efficient long-term density propagation featuring the highly deformed and elongated density distribution. The concept of alpha shape is included to get accurate interpolated density within the non-convex alpha shape triangulation enclosing all the samples. The improved binning method increases the density accuracy by considering the variant nonlinearity of the density within each alpha shape triangulation, which calculates the joint and marginal density as the weighted sum of density weights per bin area and per bin width, respectively. To ensure the performance of the DEE method for the long-term density propagation, the suitable values of the sample number for the dynamical propagation and the grid number for performing the linear interpolation are selected by trading off the density accuracy and the computational efficiency. The superiority of the AT-B2 method is demonstrated in terms of the density accuracy and the computational efficiency compared with that of the AT-B1 and DT-B1 methods with respect to that of the MC method, for the planar phase space long-term density propagation problem in the context of high-altitude and high area-to-mass ratio satellite long-term density propagation.

Acknowledgments The work has received funding from China Scholarship Council (CSC No. 202006830123), 2020 Postgraduate Research Practice Innovation Program of Jiangsu Province (Grant No. KYCX20_0222). Pan Sun and Shuang Li fully appreciate their financial supports.

Author contributions SP wrote the main manuscript, and all authors reviewed the manuscript.

Declarations

Conflict of interest The authors declare no competing interests.

Appendix A: Scenario 2, $t = 1.5$ yrs

For the case Scenario 2, $t = 1.5$ yrs, for the AT method, the compact alpha shape triangulation enclosing all the samples is generated for a predefined alpha radius $r_a = 8$. Figure 8 presents the illustration and comparison for the DT and AT methods for the case $N_{sam} = 961$ for Scenario 2, $t = 1.5$ yrs in the solar angle-eccentricity 2D phase space. The values of the sample number and the grid number are selected as $N_{sam} = 2000$, $Ngrid = 1000$ for the AT-B2 method, by trading off the density accuracy and the computational efficiency. Figure 9 presents the evolution of the normalized LD measure for the joint and marginal density with N_{sam}, and with $Ngrid$, respectively, for AT-B2, AT-B1 and DT-B1 methods, with respect

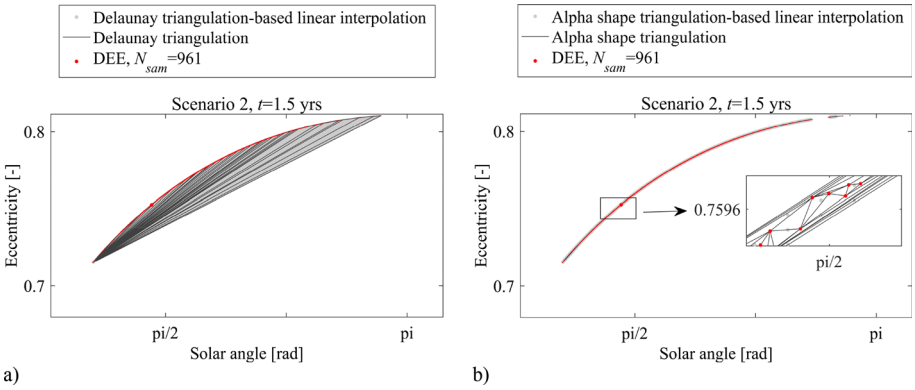

Fig. 8 Illustration and comparison for the (**a**) DT and (**b**) AT methods for Scenario 2, $t = 1.5$ yrs ($N_{sam} = 961$)

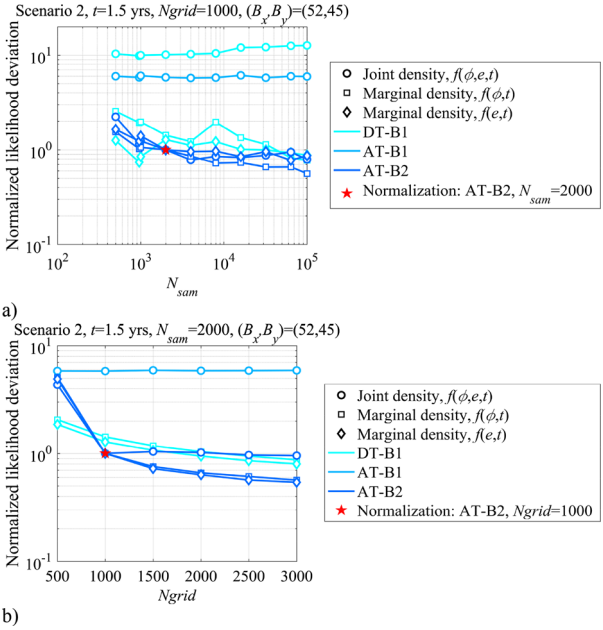

Fig. 9 Normalized LD evolution (**a**) with N_{sam}, and (**b**) with $Ngrid$, for DEE methods, with respect to the case AT-B2 ($N_{sam} = 2000$, $Ngrid = 1000$), for Scenairo 2, $t = 1.5$ yrs

to the case AT-B2 ($N_{sam} = 2000$, $Ngrid = 1000$). Figure 10 gives the evolution of the normalized performance index with N_{sam}, and with $Ngrid$, respectively, with respect to the case AT-B2 ($N_{sam} = 2000, Ngrid = 1000$). Figure 11 presents the evolution of the normalized computational effort with N_{sam}, and with $Ngrid$, respectively, with respect to that of the MC method. For the selected sample number and the grid number $\{N_{sam} = 2000, Ngrid = 1000\}$ for the case Scenario 2, $t = 1.5$ yrs, we present the joint and marginal density in Figs. 12 and 13, for the AT-B2 method compared with the AT-B1, DT-B1 methods with respect to that of the MC method.

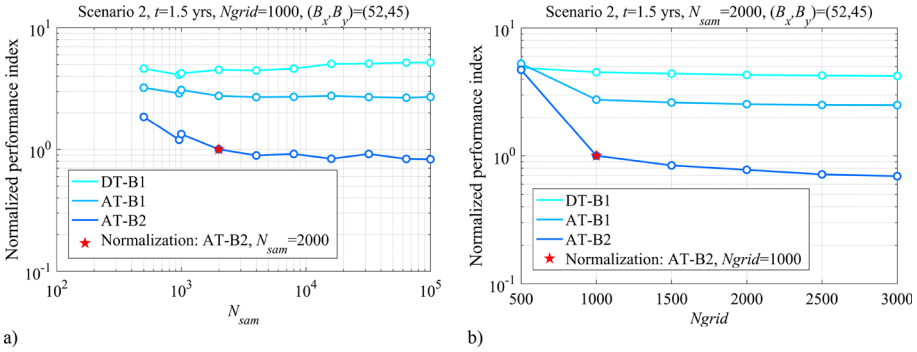

Fig. 10 Normalized performance index J_p evolution (**a**) with N_{sam}, and (**b**) with $Ngrid$, for DEE methods, with respect to the case AT-B2 ($N_{sam} = 2000$, $Ngrid = 1000$), for Scenario 2, $t = 1.5$ yrs

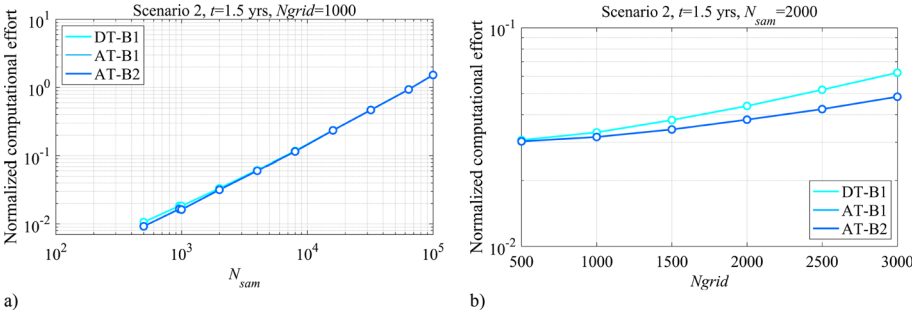

Fig. 11 Normalized computational effort evolution (**a**) with N_{sam}, and (**b**) with $Ngrid$, for DEE methods, with respect to the MC method, for Scenario 2, $t = 1.5$ yrs

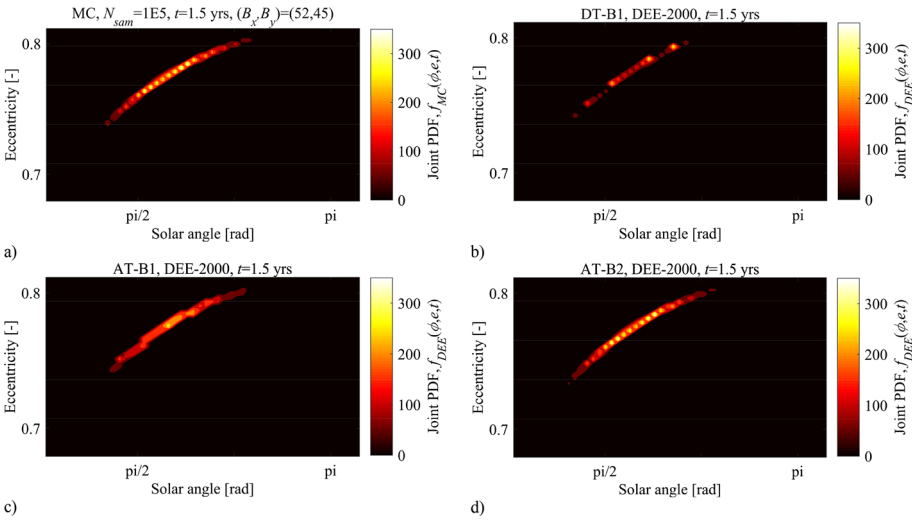

Fig. 12 The joint density (**a**) for the MC method; (**b**) for the DT-B1 method, (**c**) for the AT-B1 method, (**d**) for the AT-B2 method, with $\{N_{sam} = 2000, Ngrid = 1000\}$ (for Scenario 2, $t = 1.5$ yrs)

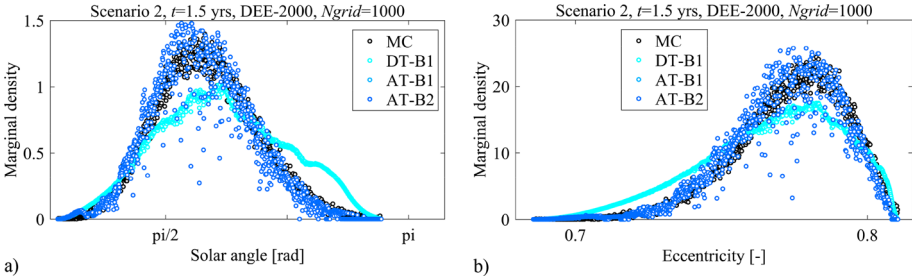

Fig. 13 The marginal density of the (**a**) solar angle, (**b**) and the eccentricity with $\{N_{sam} = 2000, Ngrid = 1000\}$, for DT-B1, AT-B1 and AT-B2 methods with respect to the MC method, for Scenario 2, $t = 1.5$ yrs

Appendix B: Scenario 2, $t = 3$ yrs

For the case Scenario 2, $t = 3$ yrs, for the AT method, the compact alpha shape triangulation enclosing all the samples is generated for a predefined alpha radius $r_a = 0.03$. Figure 14 presents the illustration and comparison for the DT and AT methods for the case $N_{sam} = 961$ for Scenario 2, $t = 3$ yrs in the solar angle-eccentricity 2D phase space. The values of the sample number and the grid number are selected as $N_{sam} = 2000$, $Ngrid = 1000$ for the AT-B2 method, by trading off the density accuracy and the computational efficiency. Figure 15 presents the evolution of the normalized LD measure for the joint and marginal density with N_{sam}, and with $Ngrid$, respectively, for AT-B2, AT-B1 and DT-B1 methods, with respect to the case AT-B2 ($N_{sam} = 2000$, $Ngrid = 1000$). Figure 16 gives the evolution of the normalized performance index with N_{sam}, and with $Ngrid$, respectively, with respect to the case AT-B2 ($N_{sam} = 2000$, $Ngrid = 1000$). Figure 17 presents the evolution of the normalized computational effort with N_{sam}, and with $Ngrid$, respectively, with respect to

that of the MC method. For the selected sample number and the grid number $\{N_{sam} = 2000, Ngrid = 1000\}$ for the case Scenario 2, $t = 3$ yrs, we present the joint and marginal density in Figs. 18 and 19, for the AT-B2 method compared with the AT-B1, DT-B1 methods with respect to that of the MC method.

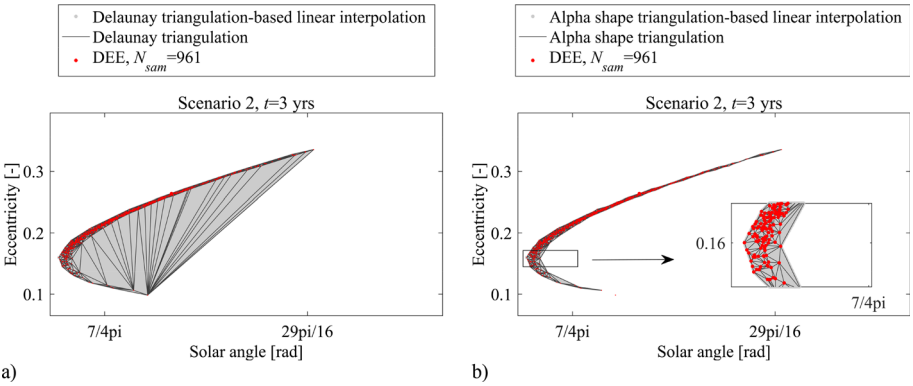

Fig. 14 Illustration and comparison for the (**a**) DT and (**b**) AT methods for Scenario 2, $t = 3$ yrs ($N_{sam} = 961$)

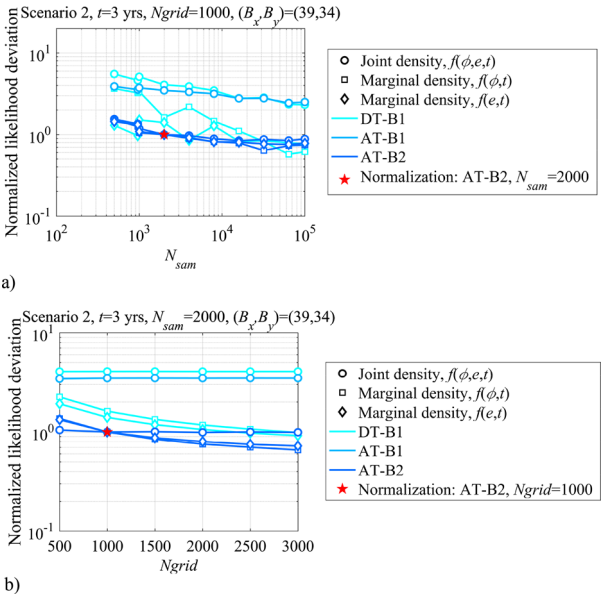

Fig. 15 Normalized LD evolution (**a**) with N_{sam}, and (**b**) with $Ngrid$, for DEE methods, with respect to the case AT-B2 ($N_{sam} = 2000$, $Ngrid = 1000$), for Scenairo 2, $t = 3$ yrs

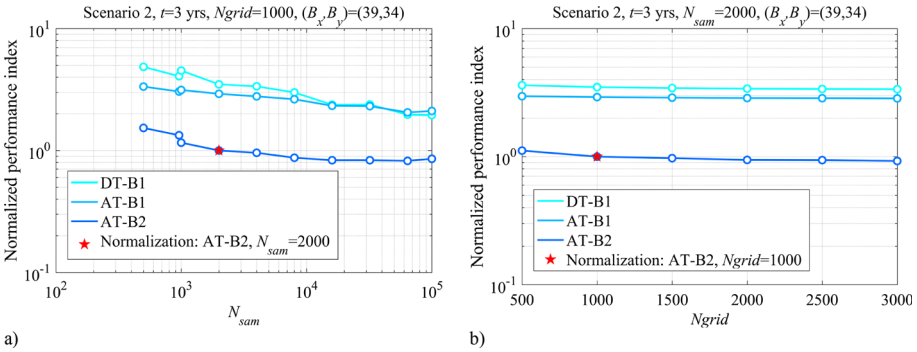

Fig. 16 Normalized performance index J_p evolution (**a**) with N_{sam}, and (**b**) with $Ngrid$, for DEE methods, with respect to the case AT-B2 ($N_{sam} = 2000$, $Ngrid = 1000$), for Scenario 2, $t = 3$ yrs

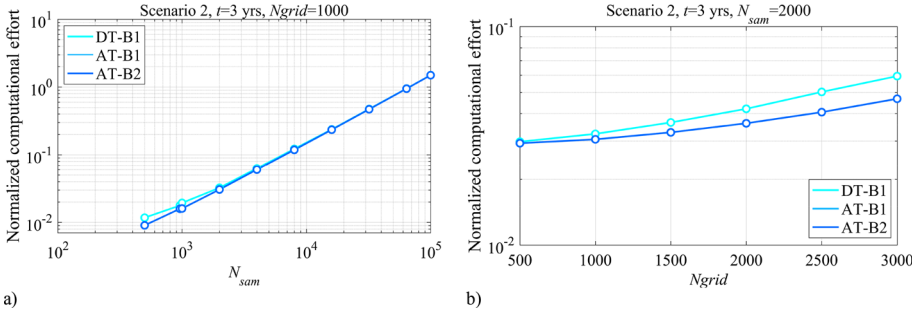

Fig. 17 Normalized computational effort evolution (**a**) with N_{sam}, and (**b**) with $Ngrid$, for DEE methods, with respect to the MC method, for Scenario 2, $t = 3$ yrs

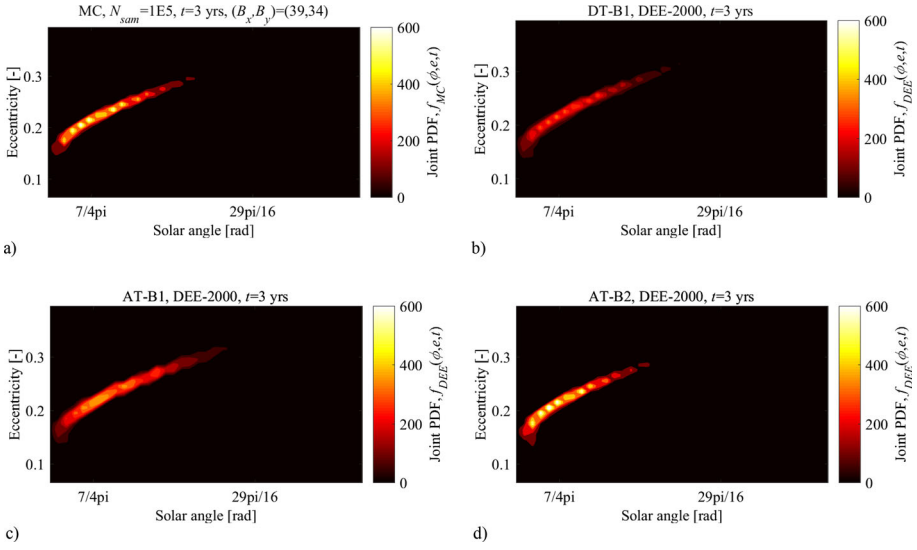

Fig. 18 The joint density (**a**) for the MC method; (**b**) for the DT-B1 method, (**c**) for the AT-B1 method, (**d**) for the AT-B2 method, with $\{N_{sam} = 2000, Ngrid = 1000\}$ (for Scenario 2, $t = 3$ yrs)

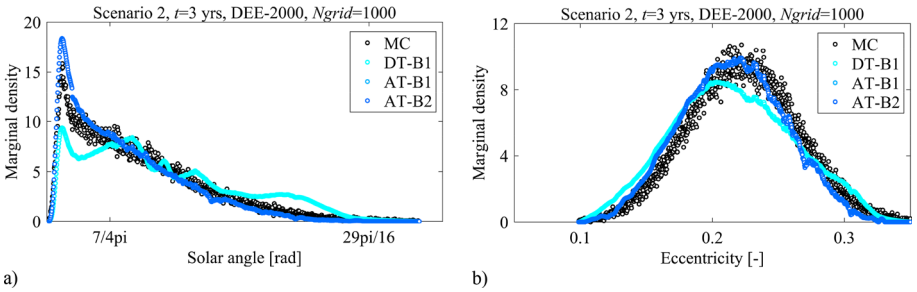

Fig. 19 The marginal density of the (**a**) solar angle, (**b**) and the eccentricity with $\{N_{sam} = 2000, Ngrid = 1000\}$, for DT-B1, AT-B1 and AT-B2 methods with respect to the MC method, for Scenario 2, $t = 3$ yrs

References

Colombo, C., McInnes, C.R.: Evolution of swarms of 'smart dust' spacecraft. New Trends in Astrodynamics and Applications VI, New York (2011)

Evans, L. C.: Partial differential equations. Grad. Stud. Math. **19**(2) (1998)

Edelsbrunner, H., Mücke, E.P.: Three-dimensional alpha shapes. ACM Trans. Graph. **13**(1), 43–72 (1994). https://doi.org/10.1145/174462.156635

Feng, J., Santeramo, D., Di Lizia, P., Armellin, R., Hou, X.: Dynamical structure of the motion around asteroids with uncertain gravity and solar radiation pressure. Acta Astronaut. **186**, 135–147 (2021). https://doi.org/10.1016/j.actaastro.2021.05.023

Frey, S.: Evolution and hazard analysis of orbital fragmentation continua. Doctoral thesis. Politecnico di Milano. Supervisors: Colombo, C., Lemmens, S., Krag, H. pp. 31–32 (2020)

Giza, D., Singla, P., Jah, M.: An approach for nonlinear uncertainty propagation: application to orbital mechanics. AIAA Guidance, Navigation, and Control Conference, AIAA Paper 2009–6082 (2009). https://doi.org/10.2514/6.2009-6082

Gor'kavyi, N.N., Ozernoy, L.M., Mather, J.C., Taidakova, T.: Quasi-stationary states of dust flows under Poynting-Robertson drag: New analytical and numerical solutions. Astrophys. J. **488**(1), 268–276 (1997). https://doi.org/10.1086/304702

Gor'kavyi, N.N., Ozernoy, L.M., Mather, J.C.: A new approach to dynamic evolution of interplanetary dust. Astrophys. J. **474**(1), 496–502 (1997). https://doi.org/10.1086/303440

Halder, A., Bhattacharya, R.: Dispersion analysis in hypersonic flight during planetary entry using stochastic Liouville equation. J. Guid. Control. Dyn. **34**(2), 459–476 (2016). https://doi.org/10.2514/1.51196

Jia, B., Xin, M.: Short-arc orbital uncertainty propagation with arbitrary polynomial chaos and admissible region. J. Guid. Control. Dyn. **43**(4), 715–728 (2020). https://doi.org/10.2514/1.g004548

Krivov, A.V., Getino, J.: Orbital evolution of high-altitude balloon satellites. Astron. Astrophys. **318**, 308–314 (1997)

Letizia, F., Colombo, C., Lewis, H.G.: Analytical model for the propagation of small-debris-object clouds after fragmentations. J. Guid. Control. Dyn. **38**(8), 1478–1491 (2015). https://doi.org/10.2514/1.G000695

Letizia, F., Colombo, C., Lewis, H.G.: Multidimensional extension of the continuity equation method for debris clouds evolution. Adv. Space Res. **57**(8), 1624–1640 (2016a). https://doi.org/10.1016/j.asr.2015.11.035

Letizia, F., Colombo, C., Van den Eynde, J., Armellin, R., Jehn, R.: SNAPPSHOT: Suite for the numerical analysis of planetary protection. In 6th International Conference on Astrodynamics Tools and Techniques (ICATT). pp. 14–17 (2016b)

McInnes, C.R.: Simple analytic model of the long-term evolution of nanosatellite constellations. J. Guid. Control. Dyn. **23**(2), 332–338 (2000). https://doi.org/10.2514/2.4527

Nazarenko, A.: The development of the statistical theory of a satellite ensemble motion and its application to space debris modeling. In Proceedings of the 2nd European Conference on Space Debris, ESOC. ESA SP-393 (1997)

Preparata, F.P., Shamos, M.I.: Computational Geometry, pp. 191–218. Springer-Verlag, New York (1985)

Smirnov, N. N., Nazarenko, A. I., Kiselev, A. B.: Modelling of the space debris evolution based on continua mechanics. In the Proceedings of the 3rd European Conference on Space Debris, ESOC. ESA SP-473 (2001)

Sun, P., Colombo, C., Trisolini, M., Li, S.: Comparison of continuity equation and Gaussian mixture model for long-term density propagation using semi-analytical methods. Celest. Mech. Dyn. Astron. **134**, 22 (2022a). https://doi.org/10.1007/s10569-022-10066-8

Sun, P., Colombo, C., Trisolini, M., Li, S.: Hybrid Gaussian mixture splitting techniques for uncertainty propagation in nonlinear dynamics. J. Guid. Control. Dyn. (2022b). https://doi.org/10.2514/1.G006696

Trisolini, M., Colombo, C.: Propagation and reconstruction of reentry uncertainties using continuity equation and simplicial interpolation. J. Guid. Control. Dyn. **44**(4), 793–811 (2021). https://doi.org/10.2514/1.G005228

Wittig, A., Colombo, C., Armellin, R.: Long-term density evolution through semi-analytical and differential algebra techniques. Celest. Mech. Dyn. Astron. **128**(4), 435–452 (2017). https://doi.org/10.1007/s10569-017-9756-x

Wittig, A., Di Lizia, P., Armellin, R., Makino, K., Bernelli-Zazzera, F., Berz, M.: Propagation of large uncertainty sets in orbital dynamics by automatic domain splitting. Celest. Mech. Dyn. Astron. **122**(3), 239–261 (2015). https://doi.org/10.1007/s10569-015-9618-3